PCCP

Accepted Manuscript

This is an *Accepted Manuscript*, which has been through the Royal Society of Chemistry peer review process and has been accepted for publication.

Accepted Manuscripts are published online shortly after acceptance, before technical editing, formatting and proof reading. Using this free service, authors can make their results available to the community, in citable form, before we publish the edited article. We will replace this *Accepted Manuscript* with the edited and formatted *Advance Article* as soon as it is available.

You can find more information about *Accepted Manuscripts* in the Information for Authors.

Please note that technical editing may introduce minor changes to the text and/or graphics, which may alter content. The journal's standard Terms & Conditions and the Ethical guidelines still apply. In no event shall the Royal Society of Chemistry be held responsible for any errors or omissions in this *Accepted Manuscript* or any consequences arising from the use of any information it contains.

ROYAL SOCIETY OF CHEMISTRY

www.rsc.org/pccp

Exploring the Binding Mechanisms of MIF to CXCR2 by Theoretical Approaches

Lei Xu[a], Youyong Li[b], Dan Li[a], Peng Xu[c], Sheng Tian[b], Huiyong Sun[b], Hui Liu[a], Tingjun Hou[a*]

[a]College of Pharmaceutical Sciences, Zhejiang University, Hangzhou, Zhejiang 310058, China

[b]Institute of Functional Nano & Soft Materials (FUNSOM), Soochow University, Suzhou, Jiangsu 215123, China.

[c]Department of Orthopedics, Second Military Medical University affiliated Changzheng Hosipital, Shanghai, 200003, China

Corresponding author:

Tingjun Hou

E-mail: tingjunhou@zju.edu.cn or tingjunhou@hotmail.com

Phone: +86-571-88208412

Keywords: G-protein-coupled-receptor (GPCR); Macrophage migration inhibitory factor (MIF); Homology modeling; Protein-protein interactions; ZDOCK; Molecular dynamics (MD); MM/GBSA; Dynamic cross-correlation map (DCCM)

Physical Chemistry Chemical Physics Accepted Manuscript

For Table of Contents Use Only

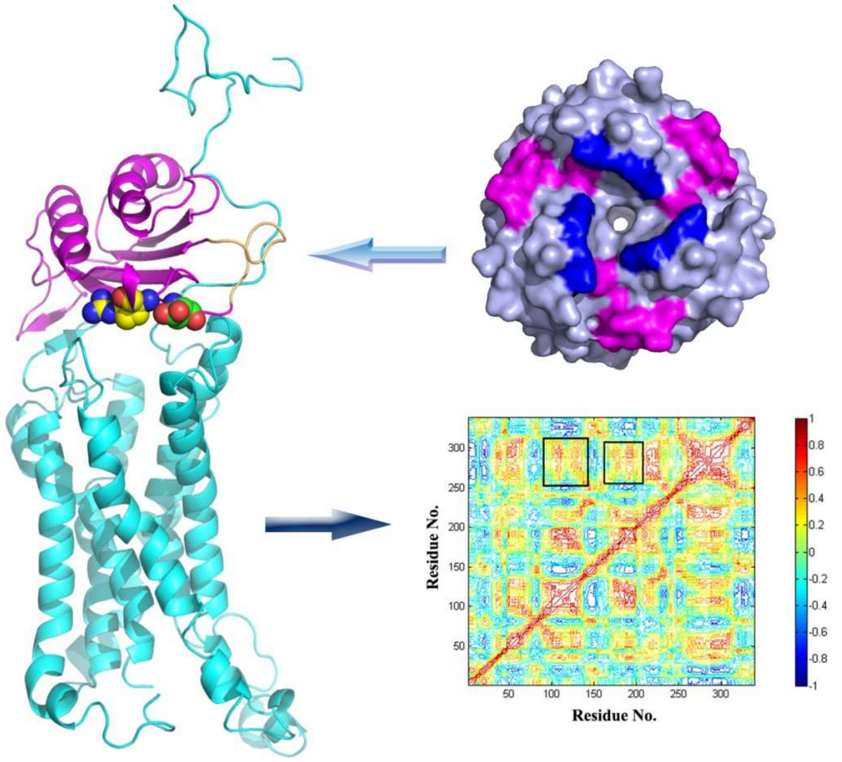

Physical Chemistry Chemical Physics Accepted Manuscript

Physical Chemistry Chemical Physics Accepted Manuscript

Abstract

Macrophage migration inhibitory factor (MIF) is a multi-functional protein that acts as a cytokine and enzyme. Recently, MIF was identified as a non-canonical ligand of G protein-coupled chemokine receptor CXCR2 with low nanomolar affinity in leukocyte arrest and chemotaxis, but the precise knowledge of the molecular determinants of the MIF-CXCR2 interface has remained unknown. Therefore, we employed homology modeling, protein-protein docking, molecular dynamics (MD) simulations, Molecular Mechanics/Generalized Born Surface Area (MM/GBSA) binding free energy calculations and MM/GBSA binding free energy decomposition to obtain insights into the molecular recognition of MIF with CXCR2. The predicted binding pattern of MIF-CXCR2 is in good agreement with the experimental data and sheds light on the functional role of important MIF-CXCR2 interface residues in association with binding and signaling. According to our predictions, the R11A/D44A double mutations of MIF exhibit a pronounced defect in the binding affinity of MIF to CXCR2, resulting in large conformational changes. The potential two-site binding model for the MIF-CXCR2 recognition was proposed: initialized primarily by the non-polar interactions including the van der Waals and hydrophobic interactions, the N-terminal region of CXCR2 contacts with the N-like loop and β-sheet of MIF (site 1), and then the ECL2 and ECL3 regions of CXCR2 form strong interactions with the *pseudo-(E)LR* motif and C-terminus of MIF, which induces the molecular thermodynamic motion of TMs for signal transduction (site 2). This study will extend our understanding to the binding mechanisms of MIF to CXCR2 and provide useful information for the rational design of potent inhibitors selectively targeting the MIF-CXCR2 interactions.

Physical Chemistry Chemical Physics Accepted Manuscript

Introduction

Macrophage migration inhibitory factor (MIF) is a proinflammatory cytokine that regulates both the innate and adaptive immune responses.[1] MIF can also activate the mitogen-activated protein kinase (MAPK) cascade and counter-act the inhibitory effects of glucocorticoids within the immune system.[2] Growing evidences have highlighted the importance of MIF in tumor growth, such as control of cell proliferation and promotion of angiogenesis.[3] In addition to its physiological and pathological activities, MIF is regarded as a D-dopachrome tautomerase,[4] a phenylpyruvate tautomerase[5] and a thol-protein oxidoreductase.[6] Accordingly, MIF is recognized as an important therapeutic target for inflammatory diseases and tumors.

Cytokines usually activate signal-transduction pathways, gene transcription and the expression of downstream effector molecules by binding to cognate receptors. By binding to the extracellular domain of CD74, MIF activates the extracellular-regulated mitogen-activated protein (ERK-MAP) kinase and is associated into a signaling complex with CD44 and Src-tyrosine kinases.[7, 8] Bernhagen *et al*. reported that MIF is a noncognage ligand of the CXC chemokine receptors CXCR2 and CXCR4, and is instrumental in inflammatory leukocyte recruitment in atherosclerosis, targeting monocytes and neutrophils through CXCR2 and T cells through CXCR4. MIF can bind to CXCR2 with low nanomolar affinity and induce CXCR2-mediated leukocyte arrest and chemotaxis.[9,10] Chemokine receptors belong to the rhodopsin-like family of G-protein-coupled receptors (GPCRs) and are termed on the basis of the corresponding binding chemokines, such as CR, CCR, CXCR and CX3CR.[11] There are two subgroups of the CXC chemokines, termed as the ELR$^+$ and ELR$^-$ chemokines. Mutagenesis or alanine scanning experiments demonstrated that substitution of the ELR residues at the N terminus of the ELR$^+$ CXC chemokines, such as CXCL18, leads to a dramatic loss of CXCR2 binding affinity.[12] Recently the emerging group of 'chemokine-like function' (CLF) includes chemotactic polypeptides such as human β-defensin (HBD), which cannot be classified into

Physical Chemistry Chemical Physics Accepted Manuscript

known chemokine subfamilies owing to the lack of the prototypical N-terminal cysteine motif but exhibit structural or functional features and can signal through chemokine receptors, for instance, CCR6.[13, 14]

MIF belongs to the class of CLF chemokines, and plays a key role in the progression of atherosclerosis, including leukocyte recruitment and arrest.[15] In 2008, Weber *et al*. revealed that MIF harbored a *pseudo-(E)LR* motif (Asp-44-X-Arg-11) constituted by non-adjacent residues in neighboring loops with identical parallel spacing of the canonical ELR motif.[16] Although MIF does not share any significant sequence homology with CXCL8, the 3D structure of the MIF monomer exhibits structural homology with the CXCL8 dimer. In 2011, Kraemer *et al.* identified an N-like loop (sequence stretch 46-55) of MIF, which appears to mirror the N loop of CXCL8 (Figure 1), by applying a variety of biochemical, biophysical and functional assays associated with atherosclerotic leukocyte recruitment processes.[17]

Although the emerging importance of the MIF-CXCR2 interactions in the inflammatory pathogenesis of atherosclerosis has attracted extensive attention, the molecular details of the protein-protein interaction interface between MIF and CXCR2 have remained unknown. Based on the above experimental data, we employed a comprehensive set of computational tools to explore the MIF-CXCR2 interaction in the current study. First, homology modeling was carried out to construct the 3D model of CXCR2 based on the crystal structure of CXCR4.[18] Then, the ZDOCK approach was employed to predict the potential binding modes of the MIF monomer in complex with CXCR2. The best complex structure in each cluster and the R11A/D44A-MIF double mutant were submitted to 20 ns MD simulations and the binding affinity between MIF and CXCR2 was estimated by the Molecular Mechanics/Generalized Born Surface Area (MM/GBSA) approach. At last, MM/GBSA binding energy decomposition analysis was employed to highlight the key residues responsible for the MIF-CXCR2 interactions. We expect that this study can provide useful information in tackling the binding mechanisms of MIF to CXCR2

Physical Chemistry Chemical Physics Accepted Manuscript

Materials and Methods

Homology modeling

The 3D model of the human CXCR2 was constructed based on the structure of CXCR4 by using the *modeller* method[19] implemented in Discovery Studio (DS) molecular simulation package (version 2.5).[20] The N-terminal 26 residues (PDB entry: 3ODU) of the CXCR4 crystal structure do not have interpretable density and are presumed to be disordered.[18] So we modeled the missing N-terminal part of CXCR4 based on the NMR data of the CXCR4 N-terminus in complex with CXCL12 (PDB entry: 2K04)[21] using DS 2.5 as we did in our recent study to model the structure of CXCR4 in complex with CXCL12.[22] The amino acid sequence of human CXCR2 was retrieved from the Uniprot database (accession number: P25025), and the sequences were aligned (Figure S1) based on the sequence analysis of chemokine receptor families.[23, 24] Then, the homology model of CXCR2 was constructed based on the 3D structure of CXCR4 by using *modeller* in DS 2.5.[20] The conformations of N-terminus and extracellular loops (ECLs) were constrained by two disulfide bonds, one linking Cys39 at the N-terminal part with Cys286, and the other connecting Cys119 with Cys196 of ECL2, as indicated in the recent crystal structures of chemokine receptors.[18, 25] The final model was minimized by 10000 cycles with the CHARMM force field and implicit solvent model (generalized Born model with molecular volume) in DS 2.5.[20]

Protein-protein docking

The crystal structure of MIF was retrieved from the protein data bank (PDB entry:1LJT[26]), and chain A was kept and the other two chains were eliminated. The ZDOCK approach[27] implemented in DS 2.5 was employed to predict the structure of the MIF monomer in complex with CXCR2. ZDOCK shows good performance in the CAPRI challenge in the prediction of protein-protein complexes,[27] by adopting pairwise shape complementarity, desolvation and electrostatics as scoring functions optimized by fast Fourier transform.[28] ZDOCK can exhaustively search all rotational and translational space for a ligand protein with respect to its receptor protein.[29] Here, five important residues (Arg11, Asp44 and Leu46 for MIF, and Tyr23 and Glu198 for CXCR2) were constrained to be inside the binding interface according to the experimental data,[16, 17] and all the atoms of these residues are within the distance cutoff of 10 Å to any atom of the other protein. The ZRANK re-ranking method was then employed to re-evaluate the docked poses predicted by the ZDOCK calculations.[30] RDOCK was used to optimize and score the docked poses based on the CHARMM force field.[29] At last, 148 docked poses were structurally classified into three clusters, and the representative structure of each cluster was chosen for the following MD simulations.

Molecular dynamics (MD) simulations

For the best complex predicted by ZDOCK, the residues R11 and D44 of MIF were mutated to Ala in DS 2.5.[20] Then, four complexes, including three representative structures chosen from three clusters and one mutant were submitted to the MD simulations (Figure 2). Each complex was embedded in a periodic structure of 1-palmytoyl-2-oleoylsn-glycero-3-phosphatidylcholine (POPC), and the lipid molecules within 5 Å of the complex were eliminated in VMD.[31] Each system was then inserted into a water box (TIP3 water model)[32] and the waters within 5 Å of the lipid and protein were removed. Two Cl^- were placed in the grids with the strongest positive coulombic potentials in order to neutralize the system. The whole system includes the MIF monomer, CXCR2, lipid molecules, water molecules and counterions, with 125121, 124886, 124985 and 125105 atoms per periodic cell for four models, respectively (Figure S2), and the box size is ~110Å×110Å×110Å. The Amber ff99SB force field was employed for the complex.[33] The lipid parameters were established by Lipidbook,[34] a public database of force field parameters with special emphasis on lipid based on the general AMBER force field (gaff).[35] The particle mesh Ewald (PME) algorithm was

Physical Chemistry Chemical Physics Accepted Manuscript

employed to handle the long-rang electrostatics.[36] The whole system was first equilibrated for 1 ns with the protein fixed under constant temperature (310 K) and constant pressure (1 atm). Then, another 1 ns equilibration was carried out without any restrain. Starting from the last frame of the equilibration, 20 ns simulations were carried out. The MD simulations were performed by using the NAMD 2.9.[37] The SHAKE procedure was employed to constrain all bonds involving hydrogen atoms,[38] and the time step was set to 2 fs. Coordinate trajectories were saved every 10 ps in the process of MD runs.

MM/GBSA binding free energy calculations

To determine the most stable MIF-CXCR2 complex predicted by protein-protein docking, the binding free energy (ΔG_{bind}) for each complex was estimated by the MM/GBSA methodology based on the snapshots retrieved from the single MD trajectory of each complex, which is much faster and requires less sampling in comparison with separte-trajectory protocol.[39-45] In MM/GBSA, ΔG_{bind} was evaluated through the following equation:[46]

$$\begin{aligned}\Delta G_{bind} &= G_{complex} - G_{protein} - G_{ligand} \\ &= \Delta H \ + \Delta G_{solvation} - T\Delta S \\ &= \Delta E_{MM} + \Delta G_{GB} + \Delta G_{SA} - T\Delta S\end{aligned} \qquad (1)$$

where ΔE_{MM} is the gas-phase interaction energy between MIF and CXCR2, including the electrostatic and van der Waals energies; ΔG_{GB} and ΔG_{SA} are the polar and non-polar contributions of the desolvation free energy, respectively; $-T\Delta S$ is the change of the conformational entropy upon ligand binding[47], which was calculated by the normal-mode analysis (NMA) based on the 20 snapshots evenly extracted from the last 10 ns of each MD trajectory. The modified GB model (*igb* = 2) developed by Onufriev and coworkers was employed to estimate the electrostatic desolvation energy.[48] The exterior and solute dielectric constants were set to 80 and 4, respectively.

Physical Chemistry Chemical Physics Accepted Manuscript

Physical Chemistry Chemical Physics Accepted Manuscript

The nonpolar part of desolvation was estimated by the solvent accessible surface area (SASA) with the Laboratoire de Chimie des Polymres Organiques (LCPO) model:[49] $\Delta G_{\mathrm{SA}} = 0.0072 \times \Delta \mathrm{SASA}$. In total, 1000 snapshots extracted from the last 10 ns MD trajectory were used to calculate all energy terms.

MM/GBSA binding energy decomposition

In order to obtain the contribution of each residue to the binding free energy, MM/GBSA was employed to decompose the total binding free energy into the four contributions from individual residue-residue pairs,[50-53] including the van der Waals contribution (ΔE_{vdw}), the electrostatic contribution (ΔE_{ele}), the polar desolvation contribution (ΔG_{GB}) and the non-polar desolvation contribution (ΔG_{SA}), as shown in equation (2):

$$\begin{aligned}\Delta G_{residue-residue} &= \Delta G_{vdw} + \Delta G_{ele} + \Delta G_{solvation} \\ &= \Delta G_{vdw} + \Delta G_{ele} + \Delta G_{GB} + \Delta G_{SA}\end{aligned} \qquad (2)$$

The GB model with the GB parameters developed by Onufriev *et al.*[48] was used to calculate the electrostatic desolvatin energy (ΔG_{GB}). The exterior dielectric and solute dielectric constants were set to 80 and 4, respectively. The non-polar component of desolvation (ΔG_{SA}) was estimated by SASA through the ICOSA technique.[53] The 1000 snapshots extracted from the last 10 ns MD trajectory were used to estimate the energy terms shown in Equation 2.

Dynamic cross-correlation map (DCCM)

In order to evaluate the dynamic correlations between different protein domains, DCCM analysis was employed to compare the correlation differences for CXCR2.[20, 54] The correlation matrix was evaluated across all C_α atoms of Model 1 and its R11A/D44A-double mutant. The correlation coefficient S_{ij} between two atoms i and j over the course of the simulation trajectory is defined as:

$$S_{ij} = \frac{\left\langle \Delta r_i \cdot \Delta r_j \right\rangle}{\sqrt{\left\langle \Delta r_i \cdot \Delta r_i \right\rangle \left\langle \Delta r_j \cdot \Delta r_j \right\rangle}} \quad (3)$$

where displacement vectors Δr_i or Δr_j are the instantaneous fluctuation of the position of *i*th or *j*th atom with respect to its mean position, and the <...> represents trajectory averages. Postively correlated residues move in the same direction, *i.e.* $S_{ij} = 1$, while anticorrelated residues move in the opposite direction, *i.e.* $S_{ij} = -1$.

Results and Discussion

Construction of the 3D structural model of CXCR2

The structures of chemokine receptors have a few peculiarities that need careful considerations in comparison with most other GPCRs. For example, chemokine receptors have an unorthodox $T^{2.56}xP^{2.58}$ sequence motif for which a unique conformation is anticipated. The 3D structure of CXCR2 was constructed based on the recently elucidated crystal structure of its family member, CXCR4, in complex with a small molecule (PDB entry: 3ODU[18]). The sequence identity and similarity between CXCR2 and CXCR4 are 32.7% and 55.9%, respectively. Among the ten models generated by *modeller*, the model with the lowest probability density function (PDF) was chosen and further refined by energy minimization. The quality of the refined model was then assessed with respect to the conformation of the peptide backbone and the packing environment. Ramachandran plot suggests that the Phi/Psi angles of most residues are within the allowed ranges, and the percentage of the residues with Phi/Psi angles in the most favorable ranges is around 90%, similar to that of the template structure (Figure S3). In short, the quality of the Ramachandran plot was satisfactory for the model, and our model is reliable for further docking and MD simulations.

MIF-CXCR2 complex structures predicted by protein-protein docking.

Although MIF does not share sequence homology with CXCL8, they exhibit apparent

Physical Chemistry Chemical Physics Accepted Manuscript

Physical Chemistry Chemical Physics Accepted Manuscript

similar architectural homology. The residues Arg11 and Asp44 of MIF are located in neighboring loops in a parallel and adjacent position in 3D space to form a *pseudo-(E)LR* motif, similar to the classical ELR$^+$ motif of CXCL8. The N-like loop, which is positioned between the β2 and β3 strands of MIF and spans the residues 47-56, also resembles the N loop of CXCL8. The sequence lengths of the N-like loop of MIF and the N loop of CXCL8 are identical (10 aa), and they share leucine (or isoleucine) and proline residues at the start and end, respectively, but their sequences only show limited similarity. Similar to CXCL8, MIF also contains several polarized or charged residues in the interface, though the MIF N-like loop does not possess any basic residues. In overall, the distribution of the electrostatic potentials of the supposed receptor binding interface of MIF is somewhat similar to that of CXCL8. Surface topology analysis of the MIF trimer structure exhibits that the N-like loop is readily solvent exposed and therefore associated with the receptor interactions of the trimeric MIF. In fact, the N-like loop regions of the trimeric MIF seem to form radius arm-like extensions around an adhesive center composed of the *pseudo-(E)LR* motif and they may be responsible for the elaborated potential interactions with a receptor (Figure 1).

Three representative binding structures chosen from the three clusters predicted by protein-protein docking are shown in Figure 2. Model I chosen from cluster 1 has a docking score of -29.16, while Model II and Model III have the scores of 1.73 and -0.17, respectively. Mutant is the R11A/D44A-MIF double mutant of Model I. Electrostatic potential (EP) surface analysis was employed to investigate electrostatic complementarity for the binding interface of a MIF-CXCR2 complex. The EPs were predicted by *Delphi*. Based on the results of the EP surface analysis, the N-terminal residues and extracellular loops of CXCR2 show strongly negative potentials, primarily contributed from Glu2, Asp3, Glu7, Asp9, Glu12, Asp13, Glu18, Asp19, Asp35, Glu198, Asp199, Asp274, Glu284, Glu287 and Asp293, while MIF shows obviously positive potentials, mainly contributed from the positively charged side chains of several basic residues (Arg11, Lys32, His40, His62 and Lys66). Therefore, the electrostatic complementarity of the MIF surface-exposed residues and the CXCR2 N terminus and extracellular loops are important for the interaction of MIF-CXCR2, though may not be as crucial as CXCR2 with its canonical ligand CXCL8 with more basic residues.

MD simulations and MM/GBSA calculations.

Three different binding structures predicted by protein-protein docking, as well as the R11A/D44A-MIF double mutant of Model I, were submitted for the further MD simulations in explicit aqueous solution to identify the potential near-native structure of MIF with CXCR2. The RMSD values for the C_α atoms of MIF with CXCR2 during the production phase relative to the starting structures are shown in Figure 3. The averaged C_α RMSDs for four models are 4.15, 6.04, 4.80 and 6.32 Å, respectively. Model I exhibits less fluctuation in comparison with Model II and Model III, and reaches equilibrium after ~10 ns. However, the conformation of mutant changes dramatically with respect to the initial structure, indicating that the substitution of these residues has much unfavorable impact on the binding of MIF to CXCR2, which is in agreement with the experimental evidences.[16] A detailed analysis of the main chain root mean square fluctuation (RMSF) *versus* the residue number of CXCR2 is shown in Figure 4. The RMSF plot indicates that TM3, ECL2 and ECL3 show relatively smaller fluctuations due to the major interaction with MIF, whereas TM5 and TM6 show relatively larger fluctuations. The region around the residues Val187 and Gln280 are more rigid due to the direct interaction with MIF.

The MM/GBSA method was employed to estimate the absolute binding free energies for the four models. As shown in Table 1, Model I, with the lowest energy (ΔG_{pred} = -210.44 kcal/mol), is more stable than the others. Compared with Model I, mutant shows a much higher energy (ΔG_{pred} = -136.48 kcal/mol), suggesting that the R11A/D44A double mutations severely impair the binding of MIF to CXCR2.

Physical Chemistry Chemical Physics Accepted Manuscript

Physical Chemistry Chemical Physics Accepted Manuscript

According to the data shown in Table 1, the rank of the binding free energies for Model I, Model II and Model III is consistent with that of the protein-protein docking scores. Table 1 shows that the van der Waals and electrostatic terms are the primary favorable components to the MIF-CXCR2 interaction, especially the former. The non-polar solvation term, which corresponds to the burial of SASA upon binding, contribute slightly favorably, whereas the polar solvation term obviously opposes the binding.

Conformational change of MIF-CXCR2 during MD simulations.

According to the conformational change of the MIF-CXCR2 complex shown in Figure 5, CXCR2 has a higher fluctuation due to the higher dynamic feature of the CXCR2 N-terminus. The average C_α RMSDs for MIF, CXCR2, complex and the CXCR2 N-terminal region are 3.91, 5.96, 5.00, and 9.68 Å, respectively. As shown in Figure 6, compared with the other TMs, TM1, TM4 and TM5 exhibit more fluctuations. The intracellular part of TM1 moves to TM7 for ~6 Å. TM4 undergoes a clockwise rotation, and its intracellular part moves inward ~5 Å. The intracellular part of TM5 moves to TM6 for ~5 Å (Figure S4). The averaged C_α RMSDs for TM1, TM4 and TM5 are 4.0, 3.8 and 3.5 Å, respectively. TM2, TM3, TM6 and TM7 can also undergo movement, and the average C_α RMSDs of them are 2.3, 2.9, 1.8 and 2.8 Å, respectively.

Then the averaged conformation of Model I generated from the last 10 ns MD trajectory was analyzed. According to the energy components of the binding free energies in Table 1, the electrostatic interaction is important for the binding of MIF with CXCR2. Thus, the important hydrogen-bonding interactions with the key residues on the binding interface of MIF-CXCR2 over the MD simulations are illustrated in Table 2. Asp44 in the *pseudo-(E)LR* motif of MIF forms a H-bond with Gln280 of the CXCR2 ECL3 domain (15.11% occupancy). The side chain of Gln45 forms a stable H-bond with Glu284 (32.63% occupancy). Leu46 in the N-like loop of

Physical Chemistry Chemical Physics Accepted Manuscript

MIF can also form a stable H-bond with Gln283 of the CXCR2 ECL2 domain (50.32% occupancy), which are in good agreement with the previous mutational analyses.[16, 17] Cys39, which is located in the CXCR2 N-terminus and forms a disulfide bond with Cys286 at the tip of the helix VII, forms a stable H-bond with Asn6 (31.05% occupancy). The acidic residues Asn105 and Asn110 of the C-terminal region of MIF, which was demonstrated to be important in modulating the stabilization of the tertiary structure and the enzymatic activity of MIF,[55] can form H-bond interactions with Asn191 and Val187 of ECL2 (16.89% and 21.00% occupancies). Compared with the polar interactions between MIF and CXCR2, the nonpolar components, especially the van der Waals term, determine the differences of the binding affinities of the three models. The favorable nonpolar MIF-CXCR2 interactions can be explained by the structural feature of the hydrophobic residues on the protein-protein interaction interface. The lipophilicity distribution of the averaged structure for the MIF monomer with CXCR2 is shown in Figure S5. Some hydrophobic residues of the CXCR2 N-terminal region, such as Leu29, Pro30, Pro31, Phe32, Leu33, Leu34, Ala36, Ala37 and Pro38, expose outside to interact with the hydrophobic region of the N-like loop and β4 strand of the MIF monomer (Leu46, Met47, Ala48, Phe49, Pro55, Pro91, Val94 and Ile96). The Leu46 hydrophobic pocket constituted by the residues Arg11, Val14, Phe18, Leu19, Val39, His40, Val41, Val42 and Pro43 has been demonstrated to be important in stabilizing the conformation of MIF in solution, and the substitution of Leu46 can perturb the secondary and tertiary structure of the protein but do not influence the oligomerization state of MIF.[56] In addition, the hydrophobic residues of the CXCR2 ECL2 region, such as Val187 and Val192, can form favorable van der Waals interactions with the highly conserved (>95%) C-terminal region of MIF across different species,[55] such as Met101, Ala103, Ala104, Val106, Gly107 and Trp108.

Identification of the 'hot spot' residues responsible for MIF-CXCR2 interactions

Physical Chemistry Chemical Physics Accepted Manuscript

and their plausible binding mode.

The interaction spectra for MIF with CXCR2 were gained and the numerical data are illustrated in Tables S1 and S2. The plausible binding mode of the MIF-CXCR2 complex was obtained over the last 10 ns MD trajectory (Figure 7). According to the interaction spectra (Figure 8), the residues Thr28, Leu33, Pro38, Cys39, Tyr188 and Gln283, which are located in the N-terminus, ECl2 and ECl3 of CXCR2, show the largest contributions to the binding free energy, suggesting that these residues are important for the MIF binding. These computational results are consistent with the experimental findings that the N domain and ECLs of CXCR2, especially ECL2 and ECL3 form strong interaction with MIF.[17] The energy contribution of Leu33 is -7.08 kcal/mol, which is primarily coming from the van der Waals term (-6.44 kcal/mol). Leu33 can form favorable van der Waals interaction with some hydrophobic residues, including Ala48 and Phe49 of the MIF N-like loop.[17] As shown in Table S2, the energy contribution of Phe49 is -6.42 kcal/mol, primarily contributed from the van der Waals component (-6.20 kcal/mol).

According to Table 2, the acidic residue Glu40 of the CXCR2 N-terminus forms a stable H-bond with Ser60, and a salt-bridge with His62. The energy contribution of Glu40 is -3.26 kcal/mol, which is primarily coming from the electrostatic term (-14.88 kcal/mol), though it can be tremendously counteracted by the polar desolvation term. As shown in Table 2, the backbone of Val187 of ECL2 forms a H-bond with Asn110. The electrostatic term of the Val187 is -1.64 kcal/mol, and the energy contribution of Asn110 is -16.4 kcal/mol, which is primarily contributed from the electrostatic term (-39.58 kcal/mol). Figure 7 shows that Tyr188 of ECL2 can form aryl-aryl interaction with Trp108 in a T-shaped geometry. The energy contribution of Tyr188 is -10.14 kcal/mol, which is mainly coming from the van der Waals term (-9.82 kcal/mol). Table 2 shows that the acid residue Gln280 in ECL3 can form a H-bond with Asp44 of the MIF *pseudo-(E)LR* motif, which is critical for the MIF binding to ECL2 and ECL3 based on the peptide array analysis.[17] The energy contribution of Gln280 is

Physical Chemistry Chemical Physics Accepted Manuscript

-2.74 kcal/mol, which is mainly contributed from the electrostatic term (-2.3 kcal/mol), while the energy contribution of Asp44 is -2.6 kcal/mol, primarily coming from the electrostatic term (-4.38 kcal/mol) as well. The backbone of Gln283 also forms a stable H-bond with Leu46 of the MIF N-like loop. The energy contribution of Gln283 is -6.48 kcal/mol, and the electrostatic term is -2.94 kcal/mol. In addition, the side chain of Gln283 can form hydrophobic interactions with Val42, Pro43 and Leu46, and its van der Waals contribution is -5.55 kcal/mol.

The Leu46 hydrophobic pocket plays a key role in stabilizing the conformation of MIF, and Arg11 is an important component of the Leu46 hydrophobic site and forms a sort of a "cap" to the pocket.[56] The energy contribution of Leu46 is -8.58 kcal/mol, which is mainly coming from the nonpolar interaction energy term (-8.74 kcal/mol). The backbone of Gln284 forms a stable H-bond with Gln45, and the electrostatic energy term of Gln284 is -3.66 kcal/ mol.

Comparison of the structures of CXCR2 with wild-type MIF and R11A/D44A-MIF double mutant

To gain insights into the conformational changes caused by the R11A/D44A-MIF double mutations, dynamic cross-correlation maps analysis was performed, and the correlation coefficients of the different regions of CXCR2 are shown in Figure 9. Apparently, there are conformational couplings between ECLs and TMs, including ECL2 with TM6 and TM7, and ECL3 with TM3 and TM4. Compared with the wide-type (WT) complex, the mutant shows a general increase in residue-residue correlations (Figure 9b). Moreover, it seems that the mutations affect the correlation of those residues that are spatially apart. In the case of WT, small values are found around the residues 100-140 (TM3 and ECL1) and residues 250-320 (TM6, TM7 and ECL3). However, these couplings are obviously increased when Arg11 and Asp44 are substituted to Ala. The increased residue-residue correlations suggest that the flexibility resulted from the mutations around the mutated sites are coupled with other

Physical Chemistry Chemical Physics Accepted Manuscript

motions in the structure. Besides, the correlated motions of the mutations around the residues 160-190 (TM4 and ECL2) and 250-320 revealed a rapid increase of the correlations in comparison with WT, indicating that the R11A/D44A-MIF double mutations impair the binding affinity of MIF to CXCR2 and lead to relatively high correlations of CXCR2.

In order to further explore the effect of the mutations, the averaged structure of CXCR2 with the R11A/D44A-MIF double mutant over the last 10 ns MD trajectory was compared with that of the WT model (Model I). Mutant shows more fluctuation with the average C_α RMSD value of 6.32 Å, in comparison with Model I (4.15 Å) (Figure 3). The absolute binding free energies predicted by MM/GBSA also demonstrate that mutant is much less stable than Model I, suggesting that the substitutions of Arg11 and Asp44 by Ala severely impact the binding affinity between MIF and CXCR2, which is in good agreement with the experimental data.[16] Then the averaged structure of mutant was fitted into the averaged structure of Model I to analyze the important conformational changes on the MIF-CXCR2 binding interface. As shown in Figure 10, the key conformational changes within the binding interface include the *pseudo-(E)LR* motif and the C-terminal region of MIF with the CXCR2 ECL2 domain. In the WT model, the basic residue Arg11 can form polar interaction with the negative center of ECL2 composed of Asn202, Asn203 and Asn206. The distance between the geometric center of Arg11/Ala11 and Asn 203 was calculated during the 20 ns MD simulations to monitor the binding of MIF-CXCR2. In the WT model, the distance between Arg11 and Asn203 is gradually shortened during the stimulations, suggesting that Arg11 may form a tighter binding with the ECL2 region, while that between Ala11 and Asn203 is gradually lengthened, showing a looser binding. In addition, Trp108 of the C-terminus of MIF can form aryl-aryl interaction with Tyr188 in the WT model, which is absent in CXCR2 with the R11A/D44A-MIF double mutant, and the distance between the nitrogen atom of the indole moiety of Trp108 and the oxygen atom of the phenol group of Tyr188 changes from 5.83 to

25.20 Å.

Then, the binding free energy decomposition analyses were performed to compare which residues have significant contribution differences between MIF and CXCR2 for the WT and mutant (Figure 11). The differences of the MIF-CXCR2 residue energies were evaluated ($\Delta\Delta E = \Delta E_{\mathrm{R11A/D44A}} - \Delta E_{\mathrm{WT}}$), and a positive $\Delta\Delta E$ shows a weaker binding affinity in the mutated model, while a negative $\Delta\Delta E$ indicates a stronger binding affinity. As shown in Figures 11 and S6, the R11A/D44A mutations obviously weaken the interaction between MIF and CXCR2 in comparison with the WT model. The energy contribution of Tyr188 is -10.14 kcal/mol, mainly coming from the non-polar interaction energy term (-11.02 kcal/mol) in the WT model, which can form strong aryl-aryl interaction with Trp108 and hydrophobic interaction with Val106 of the MIF C-terminus, whereas the energy contribution of Tyr188 is reduced to -0.82 kcal/mol in the mutant (Table S3). The energy contribution of Ser189 is -5.58 kcal/mol in the WT model, which is primarily from the non-polar interaction energy term (-6.14 kcal/mol), and it can form hydrophobic interaction with Trp108, whereas the energy contribution of Ser189 is reduced to -0.92 kcal/mol in the mutant.

Binding mechanism of MIF with CXCR2.

Although the chemokine receptor can be activated by various chemokine ligands with a range of specificities and affinities, a general two-site mechanism of the ligand-receptor interaction has been recognized, including the interactions between the receptor N-domain and the ligand N-terminal loop residues (site I), and between the receptor extracellular loop and the ligand N-terminal residues (site II). The site 1 binding motif is proposed to contribute differently to binding affinity and receptor selectivity, while site 2 is responsible to control binding affinity and receptor activation. The interaction between CXCR2 and CXCL8 is also involved in the two-site binding mechanism, including the N-terminus and N loop, extracellular loop and N-terminus, respectively, especially the ELR motif.

Physical Chemistry Chemical Physics Accepted Manuscript

Physical Chemistry Chemical Physics Accepted Manuscript

As represented in the dynamic and energetic analyses mentioned above, the putative binding mechanism of MIF with CXCR2 was proposed at molecular level: primarily initialized by the non-polar interactions including the van der Waals and hydrophobic interactions, the N-terminal region of CXCR2 makes the first contact with the N-like loop and β-sheet of MIF (site 1); owing to the steric complementarity and electrostatic attraction, the ECL2 and ECL3 regions of CXCR2 form strong interaction with the *pseudo-(E)LR* motif and C-terminus of MIF, which induces the molecular thermodynamic motion of TMs for signal transduction (site 2). Some hydrophobic residues of the CXCR2 N-terminal region, including Leu29, Pro30, Pro31, Phe32, Leu33, Leu34, Ala36, Ala37 and Pro38, can form strong interactions with the hydrophobic region of the N-like loop and β4 strand of MIF (Leu46, Met47, Ala48, Phe49, Pro55, Pro91, Val94 and Ile96). The acidic residues of the CXCR2 N-terminus, including Asp19 and Glu40, can also form polar interaction with Lys77, Ser60 and His62 over the MD simulations. All these interactions result in the movement of MIF towards CXCR2, triggering the 2nd step interaction among the protein-protein binding interface. The hydrophobic residues of ECL2, such as Val187, Tyr188 and Val192, can form favorable van der Waals interactions with the C-terminal region of MIF, such as Met101, Ala103, Ala104, Val106 and Trp108. The basic residue Arg11 of the MIF *pseudo-(E)LR* motif can form strong polar interaction with the negative center of ECL2 composed of Asn202, Asn203 and Asn206. Tyr188 can form strong aryl-aryl interaction with Trp108 and hydrophobic interaction with Val106 of the MIF C-terminus. The acidic residue Asp44 can form a stable H-bond with Gln280 of ECL3. The conformational change of the CXCR2 extracellular region induces the molecular thermodynamic motion of TMs, especially TM5 and TM6.

Conclusion

In the present study, a comprehensive set of computational tools, including homology modeling, protein-protein docking, MD simulations, MM/GBSA binding free energy

Physical Chemistry Chemical Physics Accepted Manuscript

calculations and MM/GBSA binding free energy decomposition, were employed to obtain insights into the molecular recognition of MIF with CXCR2. The plausible near-native structure of MIF-CXCR2 was obtained and the 'hot-spot' residues important within the protein-protein binding interface were highlighted, which is in good agreement with the experimental data. Dynamic and energetic analyses demonstrated that the mutation of the *pseudo-(E)LR* motif of MIF severely comprise its binding to CXCR2. Moreover, the potential binding mechanism between MIF and CXCR2 was proposed, and these structural determinants may pave the way for the rational design of potent agents to target the proinflammatory MIF-CXCR2 interaction selectively by pinpointing the 'hot-spot' residues within the binding interface.

Supporting Materials

Table S1. Binding free energy contributions of the key binding-site residues of CXCR2 predicted by the binding energy decomposition (kcal/mol). **Table S2**. Binding free energy contributions of the key binding-site residues of MIF predicted by the binding energy decomposition (kcal/mol). **Table S3**. Binding free energy contributions of the key binding-site residues of CXCR2 in the mutated complex predicted by the binding energy decomposition (kcal/mol). **Figure S1.** Sequence alignment of CXCR2 (residues 1-339) and CXCR4 (PDB ID: 3ODU) used for homology modeling. **Figure S2.** MD simulation box of the MIF-CXCR2 complex, the lipid and water molecules. There are 125121 atoms in the simulation box (Model I was chosen to represent). **Figure S3.** Ramachandran plot of CXCR2 constructed by homology modeling. **Figure S4.** Comparison of the complex structure predicted by the protein-protein docking (ribbon colored in gray) and the conformation after the last 20 ns MD trajectory (ribbon colored in green). The arrow indicates the movement of TM1, TM4 and TM5. **Figure S5.** Schematic depiction of the major interactions of the averaged structure of MIF-CXCR2 over the last 10 ns MD trajectory (generated

Physical Chemistry Chemical Physics Accepted Manuscript

by the LIGPLOT program). (a) and (b) represent residues 1 to 57 and 58 to 114 of MIF respectively. **Figure S6.** Schematic depiction of the major interactions of the averaged structure of the R11A/D44A mutant of MIF with CXCR2 over the last 10 ns MD trajectory (generated by the LIGPLOT program). (a) and (b) represent residues 1 to 57 and 58 to 114 of MIF respectively.

Acknowledgment

This study was supported by the National Science Foundation of China (21173156), the National Basic Research Program of China (973 program, 2012CB932600). Supports from Priority Academic Program Development of Jiangsu Higher Education Institutes (PAPD) and Grant from Jiangsu Science and Technology Commission (BY2011131) are also appreciated.

References

1. Calandra, T.; Roger, T. Macrophage migration inhibitory factor: A regulator of innate immunity. *Nat. Rev. Immunol.* **2003,** 3, 791-800.
2. Morand, E. F.; Leech, M.; Jurgen, B. MIF: a new cytokine link between rheumatoid arthritis and atherosclerosis. *Nat Rev Drug Discov.* **2006,** 5, 399-410.
3. Hagemann, T.; Robinson, S. C.; Thompson, R. G.; Charles, K.; Kulbe, H.; Balkwill, F. R. Ovarian cancer cell-derived migration inhibitory factor enhances tumor growth, progression, and angiogenesis. *Mol. Cancer Ther.* **2007,** 6, 1993-2002.
4. Sugimoto, H.; Taniguchi, M.; Nakagawa, A.; Tanaka, I.; Suzuki, M.; Nishihira, J. Crystal structure of human D-dopachrome tautomerase, a homologue of macrophage migration inhibitory factor, at 1.54 angstrom resolution. *Biochemistry.* **1999,** 38, 3268-3279.
5. Rosengren, E.; Aman, P.; Thelin, S.; Hansson, C.; Ahlfors, S.; Bjork, P.; Jacobsson, L.; Rorsman, H. The macrophage migration inhibitory factor MIF is a phenylpyruvate tautomerase. *FEBS Lett.* **1997,** 417, 85-88.
6. Kleemann, R.; Kapurniotu, A.; Frank, R. W.; Gessner, A.; Mischke, R.; Flieger, O.; Juttner, S.; Brunner, H.; Bernhagen, J. Disulfide analysis reveals a role for macrophage migration inhibitory factor (MIF) as thiol-protein oxidoreductase. *J. Mol. Biol.* **1998,** 280, 85-102.
7. Leng, L.; Metz, C. N.; Fang, Y.; Xu, J.; Donnelly, S.; Baugh, J.; Delohery, T.; Chen, Y. B.; Mitchell, R. A.; Bucala, R. MIF signal transduction initiated by binding to CD74. *J. Exp. Med.* **2003,** 197, 1467-1476.
8. Shi, X. R.; Leng, L.; Wang, T.; Wang, W. K.; Du, X.; Li, J.; McDonald, C.; Chen, Z.; Murphy, J. W.; Lolis, E.; Noble, P.; Knudson, W.; Bucala, R. CD44 is the signaling component of the macrophage

migration inhibitory factor-CD74 receptor complex. *Immunity.* **2006,** 25, 595-606.

9. Bernhagen, J.; Krohn, R.; Lue, H.; Gregory, J. L.; Zernecke, A.; Koenen, R. R.; Dewor, M.; Georgiev, I.; Schober, A.; Leng, L.; Kooistra, T.; Fingerle-Rowson, G.; Ghezzi, P.; Kleemann, R.; McColl, S. R.; Bucala, R.; Hickey, M. J.; Weber, C. MIF is a noncognate ligand of CXC chemokine receptors in inflammatory and atherogenic cell recruitment. *Nat Med.* **2007,** 13, 587-596.

10. Fricker, S. P.; Metz, M. Chemokine receptor modeling: an interdisciplinary approach to drug design. *Future Med. Chem.* **2014,** 6, 91-114.

11. Veenstra, M.; Ransohoff, R. M. Chemokine receptor CXCR2: Physiology regulator and neuroinflammation controller? *J Neuroimmunology.* **2012,** 246, 1-9.

12. Hebert, C. A.; Vitangcol, R. V.; Baker, J. B. Scanning Mutagenesis of Interleukin-8 Identifies a Cluster of Residues Required for Receptor-Binding. *J Biol Chem.* **1991,** 266, 18989-18994.

13. Degryse, B.; de Virgilio, M. The nuclear protein HMGB1, a new kind of chemokine? *FEBS Lett.* **2003,** 553, 11-17.

14. Yang, D.; Chertov, O.; Bykovskaia, N.; Chen, Q.; Buffo, M. J.; Shogan, J.; Anderson, M.; Schroder, J. M.; Wang, J. M.; Howard, O. M. Z.; Oppenheim, J. J. beta-defensins: Linking innate and adaptive immunity through dendritic and T cell CCR6. *Science.* **1999,** 286, 525-528.

15. Noels, H.; Bernhagen, J.; Weber, C. Macrophage Migration Inhibitory Factor: A Noncanonical Chemokine Important in Atherosclerosis. *Trends Cardiovasc. Med.* **2009,** 19, 76-86.

16. Weber, C.; Kraemer, S.; Drechsler, M.; Lue, H. Q.; Koenen, R. R.; Kapurniotu, A.; Zernecke, A.; Bernhagen, J. Structural determinants of MIF functions in CXCR2-mediated inflammatory and atherogenic leukocyte recruitment. *Proc. Natl. Acad. Sci. U. S. A.* **2008,** 105, 16278-16283.

17. Kraemer, S.; Lue, H. Q.; Zernecke, A.; Kapurniotu, A.; Andreetto, E.; Frank, R.; Lennartz, B.; Weber, C.; Bernhagen, J. MIF-chemokine receptor interactions in atherogenesis are dependent on an N-loop-based 2-site binding mechanism. *FASEB J.* **2011,** 25, 894-906.

18. Wu, B. L.; Chien, E. Y. T.; Mol, C. D.; Fenalti, G.; Liu, W.; Katritch, V.; Abagyan, R.; Brooun, A.; Wells, P.; Bi, F. C.; Hamel, D. J.; Kuhn, P.; Handel, T. M.; Cherezov, V.; Stevens, R. C. Structures of the CXCR4 Chemokine GPCR with Small-Molecule and Cyclic Peptide Antagonists. *Science.* **2010,** 330, 1066-1071.

19. Sali, A.; Potterton, L.; Yuan, F.; Vanvlijmen, H.; Karplus, M. Evaluation of Comparative Protein Modeling by Modeler. *Proteins.* **1995,** 23, 318-326.

20. Ichiye, T.; Karplus, M. Collective Motions in Proteins - a Covariance Analysis of Atomic Fluctuations in Molecular-Dynamics and Normal Mode Simulations. *Proteins-Structure Function and Genetics* **1991,** 11, 205-217.

21. Veldkamp, C. T.; Seibert, C.; Peterson, F. C.; De la Cruz, N. B.; Haugner, J. C.; Basnet, H.; Sakmar, T. P.; Volkman, B. F. Structural Basis of CXCR4 Sulfotyrosine Recognition by the Chemokine SDF-1/CXCL12. *Sci Signaling.* **2008,** 1, ra4.

22. Xu, L.; Li, Y. Y.; Sun, H. Y.; Li, D.; Hou, T. J. Structural basis of the interactions between CXCR4 and CXCL12/SDF-1 revealed by theoretical approaches. *Mol Biosyst.* **2013,** 9, 2107-2117.

23. Rajasekaran, D.; Keeler, C.; Syed, M. A.; Jones, M. C.; Harrison, J. K.; Wu, D. Q.; Bhandari, V.; Hodsdon, M. E.; Lolis, E. J. A Model of GAG/MIP-2/CXCR2 Interfaces and Its Functional Effects. *Biochemistry.* **2012,** 51, 5642-5654.

24. de Kruijf, P.; Lim, H. D.; Roumen, L.; Renjaan, V. A.; Zhao, J. Q.; Webb, M. L.; Auld, D. S.;

Physical Chemistry Chemical Physics Accepted Manuscript

Physical Chemistry Chemical Physics Accepted Manuscript

Wijkmans, J.; Zaman, G. J. R.; Smit, M. J.; de Graaf, C.; Leurs, R. Identification of a Novel Allosteric Binding Site in the CXCR2 Chemokine Receptor. *Mol Pharmacol.* **2011,** 80, 1108-1118.

25. Tan, Q.; Zhu, Y.; Li, J.; Chen, Z.; Han, G. W.; Kufareva, I.; Li, T.; Ma, L.; Fenalti, G.; Li, J.; Zhang, W.; Xie, X.; Yang, H.; Jiang, H.; Cherezov, V.; Liu, H.; Stevens, R. C.; Zhao, Q.; Wu, B. Structure of the CCR5 Chemokine Receptor-HIV Entry Inhibitor Maraviroc Complex. *Science.* **2013,** 341, 1387-1390.

26. Lubetsky, J. B.; Dios, A.; Han, J. L.; Aljabari, B.; Ruzsicska, B.; Mitchell, R.; Lolis, E.; Al-Abed, Y. The tautomerase active site of macrophage migration inhibitory factor is a potential target for discovery of novel anti-inflammatory agents. *J Biol Chem.* **2002,** 277, 24976-24982.

27. Wiehe K, P. B., Mintseris J, Tong WW, Anderson R, Chen R, Weng Z. ZDOCK and RDOCK performance in CAPRI rounds 3, 4, and 5. *Proteins.* **2005,** 60:, 207-213.

28. Chen, R.; Weng, Z. P. Docking unbound proteins using shape complementarity, desolvation, and electrostatics. *Proteins.* **2002,** 47, 281-294.

29. Chen, R.; Li, L.; Weng, Z. P. ZDOCK: An initial-stage protein-docking algorithm. *Proteins.* **2003,** 52, 80-87.

30. Pierce, B.; Weng, Z. P. ZRANK: Reranking protein docking predictions with an optimized energy function. *Proteins.* **2007,** 67, 1078-1086.

31. Hsin, J.; Arkhipov, A.; Yin, Y.; Stone, J. E.; Schulten, K. Using VMD: an introductory tutorial. *Curr. Protoc. Bioinform.* **2008,** Chapter 5, Unit 5.7-Unit 5.7.

32. Jorgensen, W. L.; Chandrasekhar, J.; Madura, J. D.; Impey, R. W.; Klein, M. L. Comparison of Simple Potential Functions for Simulating Liquid Water. *J. Chem. Phys.* **1983,** 79, 926-935.

33. Hornak, V.; Abel, R.; Okur, A.; Strockbine, B.; Roitberg, A.; Simmerling, C. Comparison of multiple amber force fields and development of improved protein backbone parameters. *Proteins.* **2006,** 65, 712-725.

34. Domanski, J.; Stansfeld, P. J.; Sansom, M. S. P.; Beckstein, O. Lipidbook: A Public Repository for Force-Field Parameters Used in Membrane Simulations. *J. Membr. Biol.* **2010,** 236, 255-258.

35. Wang, J. M.; Wolf, R. M.; Caldwell, J. W.; Kollman, P. A.; Case, D. A. Development and testing of a general amber force field. *J. Comput. Chem.* **2004,** 25, 1157-1174.

36. Darden, T.; York, D.; Pedersen, L. Particle Mesh Ewald - an N.Log(N) Method for Ewald Sums in Large Systems. *J. Chem. Phys.* **1993,** 98, 10089-10092.

37. Phillips, J. C.; Braun, R.; Wang, W.; Gumbart, J.; Tajkhorshid, E.; Villa, E.; Chipot, C.; Skeel, R. D.; Kale, L.; Schulten, K. Scalable molecular dynamics with NAMD. *J. Comput. Chem.* **2005,** 26, 1781-1802.

38. J. P. Ryckaert, G. C. a. H. J. C. B. Numerical integration of the cartesian equations of motion of a system with constraints: molecular dynamics of< i> n</i>-alkanes. *J. Comput. Phys.* **1977,** 23, 327-341.

39. Hou, T.; Wang, J.; Li, Y.; Wang, W. Assessing the Performance of the MM/PBSA and MM/GBSA Methods. 1. The Accuracy of Binding Free Energy Calculations Based on Molecular Dynamics Simulations. *J. Chem. Inf. Model.* **2011,** 51, 69-82.

40. Xu, L.; Li, Y.; Li, L.; Zhou, S.; Hou, T. Understanding microscopic binding of macrophage migration inhibitory factor with phenolic hydrazones by molecular docking, molecular dynamics simulations and free energy calculations. *Mol. BioSyst.* **2012,** 8, 2260-2273.

41. Hou, T.; Yu, R. Molecular dynamics and free energy studies on the wild-type and double mutant HIV-1 protease complexed with amprenavir and two amprenavir-related inhibitors: Mechanism for binding and drug resistance. *J Med Chem.* **2007,** 50, 1177-1188.

42. Xu, L.; Sun, H.; Li, Y.; Wang, J.; Hou, T. Assessing the Performance of MM/PBSA and MM/GBSA Methods. 3. The Impact of Force Fields and Ligand Charge Models. *J. Phys. Chem. B* **2013,** 117, 8408-8421.

43. Sun, H.; Li, Y.; Tian, S.; Xu, L.; Hou, T. Assessing the Performance of MM/PBSA and MM/GBSA Methods. 4. Accuracies of MM/PBSA and MM/GBSA Methodologies Evaluated by Various Simulation Protocols using PDBbind Data Set. *Phys. Chem. Chem. Phys.* **2014**.

44. Liu, H.; Yao, X. Molecular Basis of the Interaction for an Essential Subunit PA-PB1 in Influenza Virus RNA Polymerase: Insights from Molecular Dynamics Simulation and Free Energy Calculation. *Mol. Pharmaceut.* **2009,** 7, 75-85.

45. Xue, Q.; Zhang, J. L.; Zheng, Q. C.; Cui, Y. L.; Chen, L.; Chu, W. T.; Zhang, H. X. Exploring the Molecular Basis of dsRNA Recognition by Mss116p Using Molecular Dynamics Simulations and Free-Energy Calculations. *Langmuir* **2013,** 29, 11135-11144.

46. Kollman, P. A.; Massova, I.; Reyes, C.; Kuhn, B.; Huo, S. H.; Chong, L.; Lee, M.; Lee, T.; Duan, Y.; Wang, W.; Donini, O.; Cieplak, P.; Srinivasan, J.; Case, D. A.; Cheatham, T. E. Calculating structures and free energies of complex molecules: Combining molecular mechanics and continuum models. *Acc. Chem. Res.* **2000,** 33, 889-897.

47. Wang, J.; Hou, T.; Xu, X. Recent Advances in Free Energy Calculations with a Combination of Molecular Mechanics and Continuum Models. *Curr. Comput.-Aided Drug Des.* **2006,** 2, 287-306.

48. Onufriev, A.; Bashford, D.; Case, D. A. Exploring protein native states and large-scale conformational changes with a modified generalized born model. *Proteins.* **2004,** 55, 383-394.

49. Weiser, J.; Shenkin, P. S.; Still, W. C. Approximate atomic surfaces from linear combinations of pairwise overlaps (LCPO). *J Comput Chem.* **1999,** 20, 217-230.

50. Hou, T.; Zhang, W.; Case, D. A.; Wang, W. Characterization of domain-peptide interaction interface: A case study on the amphiphysin-1 SH3 domain. *J. Mol. Biol.* **2008,** 376, 1201-1214.

51. Hou, T.; Li, Y.; Wang, W. Prediction of peptides binding to the PKA RII alpha subunit using a hierarchical strategy. *Bioinformatics.* **2011,** 27, 1814-1821.

52. Li, L.; Li, Y. Y.; Zhang, L. L.; Hou, T. J. Theoretical Studies on the Susceptibility of Oseltamivir against Variants of 2009 A/H1N1 Influenza Neuraminidase. *Journal Of Chemical Information And Modeling* **2012,** 52, 2715-2729.

53. Gohlke, H.; Kiel, C.; Case, D. A. Insights into protein-protein binding by binding free energy calculation and free energy decomposition for the Ras-Raf and Ras-RaIGDS complexes. *J. Mol. Biol.* **2003,** 330, 891-913.

54. Xue, W.; Yang, Y.; Wang, X.; Liu, H.; Yao, X. Computational Study on the Inhibitor Binding Mode and Allosteric Regulation Mechanism in Hepatitis C Virus NS3/4A Protein. *Plos One.* **2014,** 9, e87077.

55. El-Turk, F.; Cascella, M.; Ouertatani-Sakouhi, H.; Narayanan, R. L.; Leng, L.; Bucala, R.; Zweckstetter, M.; Rothlisberger, U.; Lashuel, H. A. The conformational flexibility of the carboxy terminal residues 105-114 is a key modulator of the catalytic activity and stability of macrophage migration inhibitory factor. *Biochemistry.* **2008,** 47, 10740-10756.

Physical Chemistry Chemical Physics Accepted Manuscript

56. El-Turk, F.; Fauvet, B.; Ashrafi, A.; Ouertatani-Sakouhi, H.; Cho, M. K.; Neri, M.; Cascella, M.; Rothlisberger, U.; Pojer, F.; Zweckstetter, M.; Lashuel, H. Characterization of Molecular Determinants of the Conformational Stability of Macrophage Migration Inhibitory Factor: Leucine 46 Hydrophobic Pocket. *Plos One*. **2012,** 7, e45024.

Physical Chemistry Chemical Physics Accepted Manuscript

Physical Chemistry Chemical Physics Accepted Manuscript

Legend of the figures

Figure 1. Structure and surface models of CXCL8 and MIF monomer. (a) the ELR motif located in the N-terminus and N-loop (orange) of CXCL8; (b) the electrostatic potential map of CXCL8 calculated by Delphi; (c) the *pseudo-(E)LR* motif and N-like loop (green) of MIF monomer; (d) the electrostatic potential map of MIF monomer. The equipotential contours at -1 kTe^{-1} and +1 kTe^{-1} are shown. Red indicates -1 kT/e and blue +1 kT/e; (e) Trimeric structure of MIF shown in surface mode. N-like loop reigions and *pseudo-(E)LR* motifs of the three monomers are shown in purple and blue respectively.

Figure 2. Structural view of the representative MIF-CXCR2 complexes predicted by protein-protein docking chosen from the three best binding models in three clusters and the R11A/D44A double mutant of Model I. The top view in each column shows the complex structure (MIF is colored in green and CXCR2 in red). The bottom view is the electrostatic potential maps calculated by Delphi. The equipotential contours at -1 kT/e and +1 kT/e are shown. Red indicates -1 kT/e and blue +1 kT/e.

Figure 3. RMSD of the backbone C_α atoms of the three representative models and R11A/D44A double mutant of Model I with respect to the first snapshot as a function of time.

Figure 4. RMSF of backbone atoms *versus* residue number of CXCR2.

Figure 5. RMSD of the backbone C_α atoms of the ligand (MIF), receptor (CXCR2), complex (MIF-CXCR2) and the N-terminus of CXCR2 with respect to the first snapshot as a function of time (Model I is chosen to represent).

Figure 6. RMSD of the backbone C_α atoms of CXCR2 TMs with respect to the first snapshot as a function of time.

Figure 7. The typical binding site of the averaged structure of the MIF-CXCR2 complex over the last 10 ns MD trajectory. Carbon atoms are colored in yellow and ribbon in purple for MIF, and carbon atoms are colored in green and ribbon in cyan for CXCR2.

Figure 8. Residue-residue interaction spectra for (a) CXCR2, (b) MIF, (c) the polarenergy ($\Delta E_{\text{ele}} + \Delta G_{\text{GB}}$) for CXCR2, (d) the polar energy ($\Delta E_{\text{ele}} + \Delta G_{\text{GB}}$) for MIF, (e) the non-polar energy ($\Delta E_{\text{vdw}} + \Delta G_{\text{SA}}$) for CXCR2, and (f) the non-polar energy ($\Delta E_{\text{vdw}} + \Delta G_{\text{SA}}$) for MIF.

Figure 9. Dynamic cross-correlation map (DCCM) analyses of CXCR2, for the (a) WT and (b) mutant. The color scale is shown on the right changing from red (highly positive correlations) to blue (highly negative correlations).

Figure 10. Comparison the difference between the WT (Model I) and R11A/D44A double mutant of Model I. (a) the distance between the Arg11/Ala11 of MIF and Gln203 of the CXCR2 ECL2 region during the MD simulations; (b) the superimposition of the averaged structures of Moldel I and R11A/D44A mutant of Model I. Carbon atoms and ribbon of MIF are colored in green in WT and cyan in mutant; Carbon atoms and ribbon of CXCR2 are colored in purple and green in WT, and carbon atoms and ribbon of CXCR2 are colored in yellow and cyan in mutant.

Figure 11. Differences in the contribution of the residues to the binding free energy between the WT (Model I) and R11A/D44A double mutant of Model I ($\Delta\Delta E = \Delta E_{\text{R11A/D44A}} - \Delta E_{\text{WT}}$). A positive $\Delta\Delta E$ represents a weaker binding affinity in the mutated protein, while a negative $\Delta\Delta E$ represents a stronger binding affinity.

Physical Chemistry Chemical Physics Accepted Manuscript

Table 1. The predicted binding free energies and the individual energy components for the studied systems (kcal/mol).

System	ΔE_{vdw}[a]	ΔE_{ele}[b]	ΔG_{SA}[c]	ΔG_{GB}[d]	$-T\Delta S$[e]	$\Delta E_{\mathrm{enthalpy}}$[f]	ΔG_{pred}[g,h]
Model I	-142.62±0.12[h]	-80.75±0.52	-21.4±0.07	96.55±0.38	-62.40±0.79	-148.04±0.35	-210.44±0.35
Model II	-89.56±1.54	-46.53±2.38	-13.391.33	58.11±1.34	-54.82±3.04	-91.37±3.76	-146.19±3.76
Model III	-113.34±1.07	-138.74±3.14	-20.38±0.47	147.2±1.88	-56.27±2.88	-125.22±4.26	-181.49±4.26
Mutant	-88.62±2.05	-47.39±5.01	-14.47±1.54	58.86±3.79	-44.86±6.92	-91.62±4.08	-136.48±4.08

[a] van der Waals energy
[b] Electrostatic energy
[c] Electrostatic contribution to solvation.
[d] Non-polar contribution to solvation.
[e] Entropic contribution.
[f] Binding free energy in the absence of entropic contribution.
[g] Binding free energy.
[h] Standard deviations based on two blocks (block 1: 10−15 ns, block 2: 16−20 ns).

Table 2. Hydrogen-Bond analysis based on the MD trajectories. Donor and acceptor pairs satisfy the criteria for the hydrogen bond over 15% are listed during the MD simulations. Residues of MIF are colored in red.

Donor		Acceptor		
Residue	Group	Residue	Group	Occupancy
Cys39	NH	Asn6	OD1	31.05%
Gln280	NH2	Asp44	O	15.11%
Gln45	NH2	Glu284	O	32.63%
Leu46	NH1	Gln283	O	50.32%
Ser60	OH	Glu40	OE1	70.32%
His62	NH2	Glu40	OE1	36.84%
Lys77	NH1	Asp19	OD2	20.63%
Tyr25	OH	Asp92	OD1	20.00%
Asn191	NH	Asn105	O	16.89%
Asn110	NH	val187	O	21.00%

Physical Chemistry Chemical Physics Accepted Manuscript

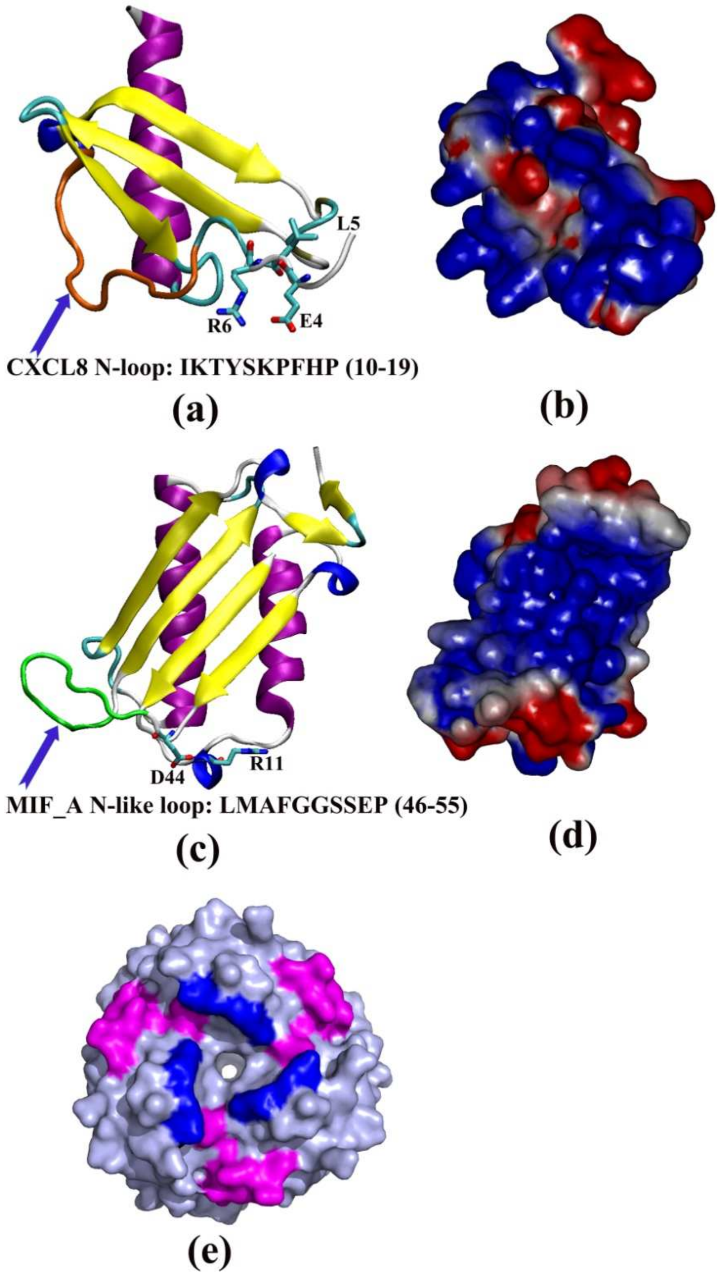

Figure 1

Physical Chemistry Chemical Physics Accepted Manuscript

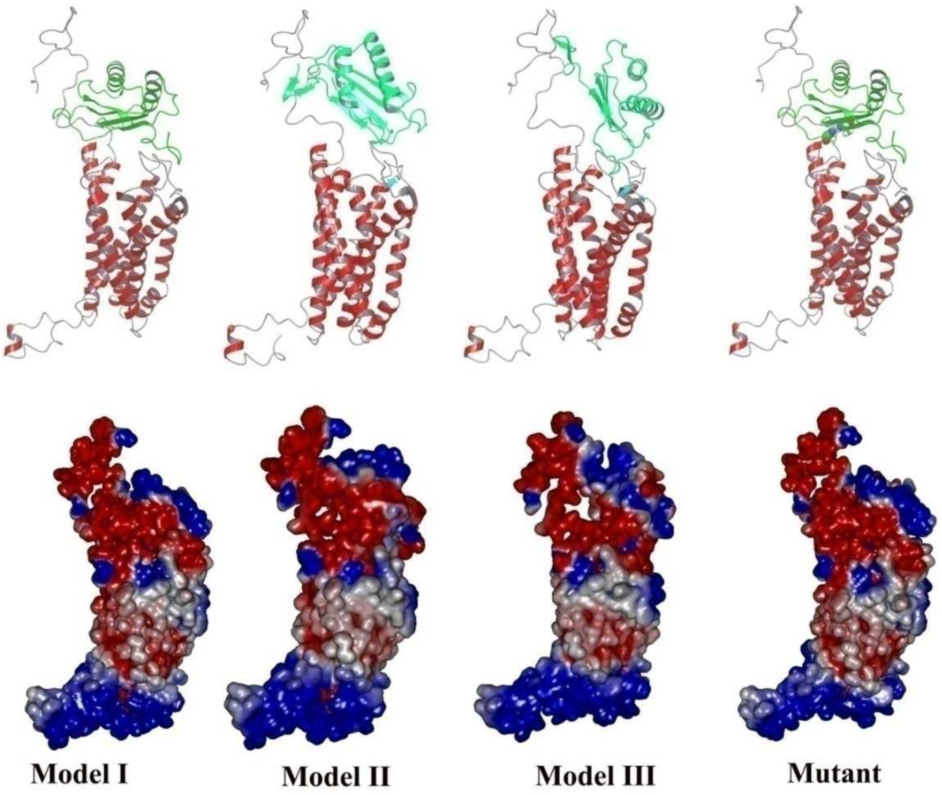

Figure 2

Physical Chemistry Chemical Physics Accepted Manuscript

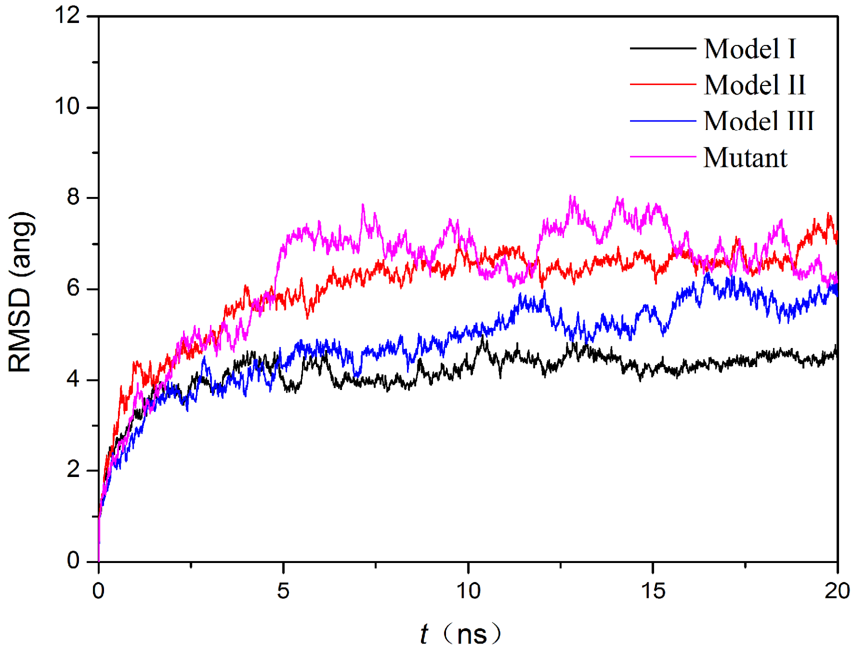

Figure 3

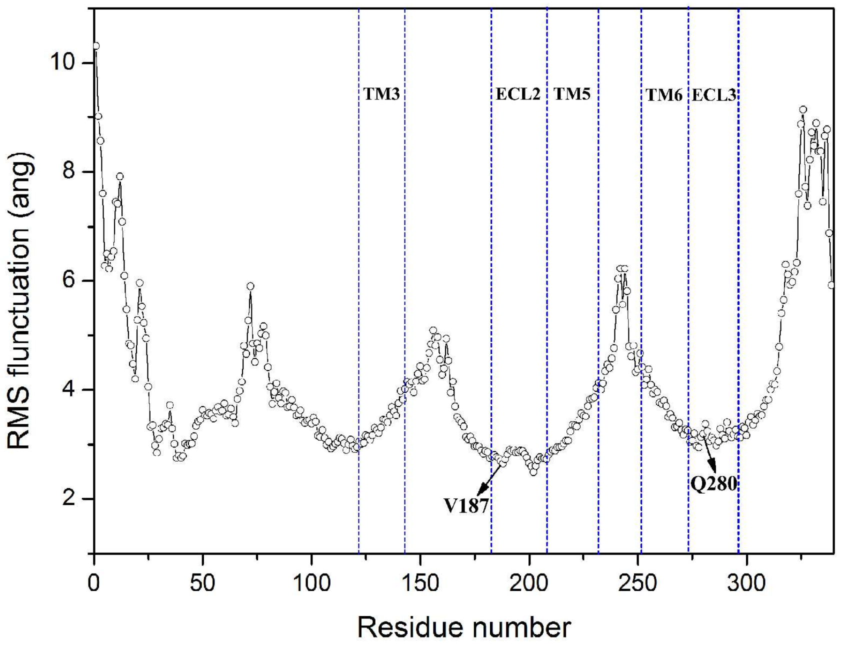

Figure 4

Physical Chemistry Chemical Physics Accepted Manuscript

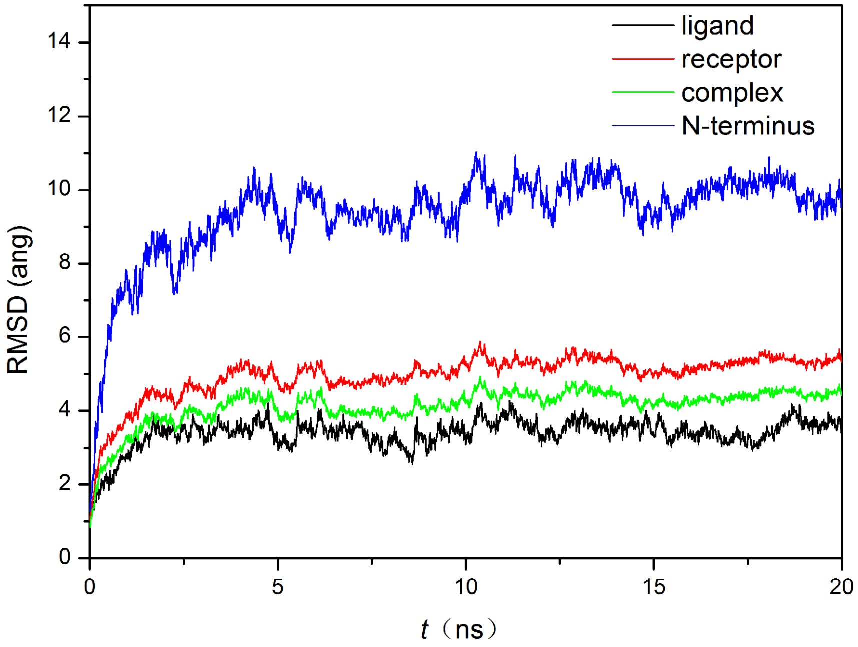

Figure 5

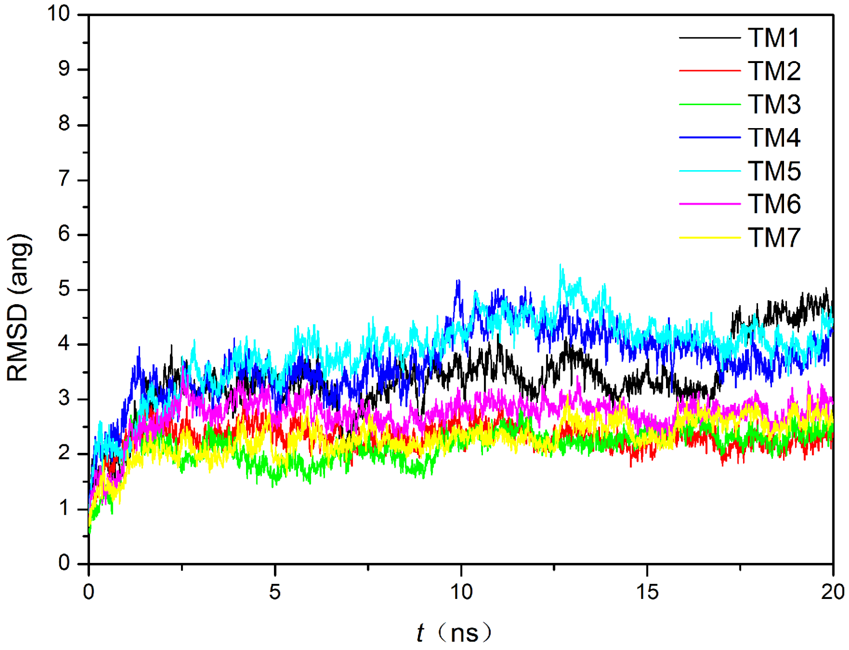

Figure 6

Physical Chemistry Chemical Physics Accepted Manuscript

Physical Chemistry Chemical Physics Accepted Manuscript

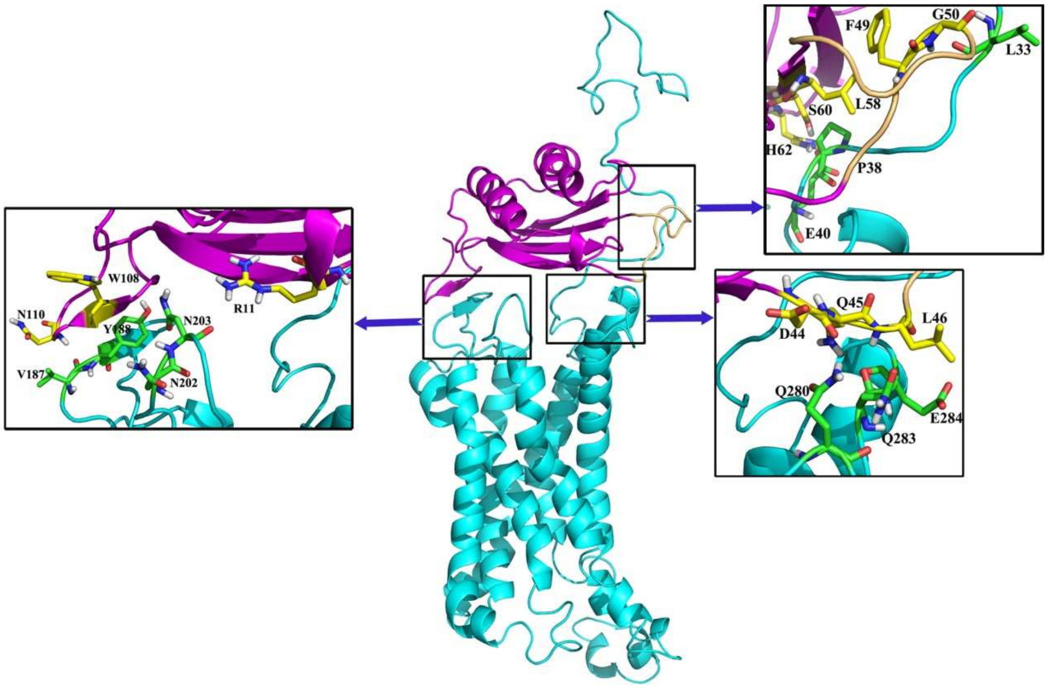

Figure 7

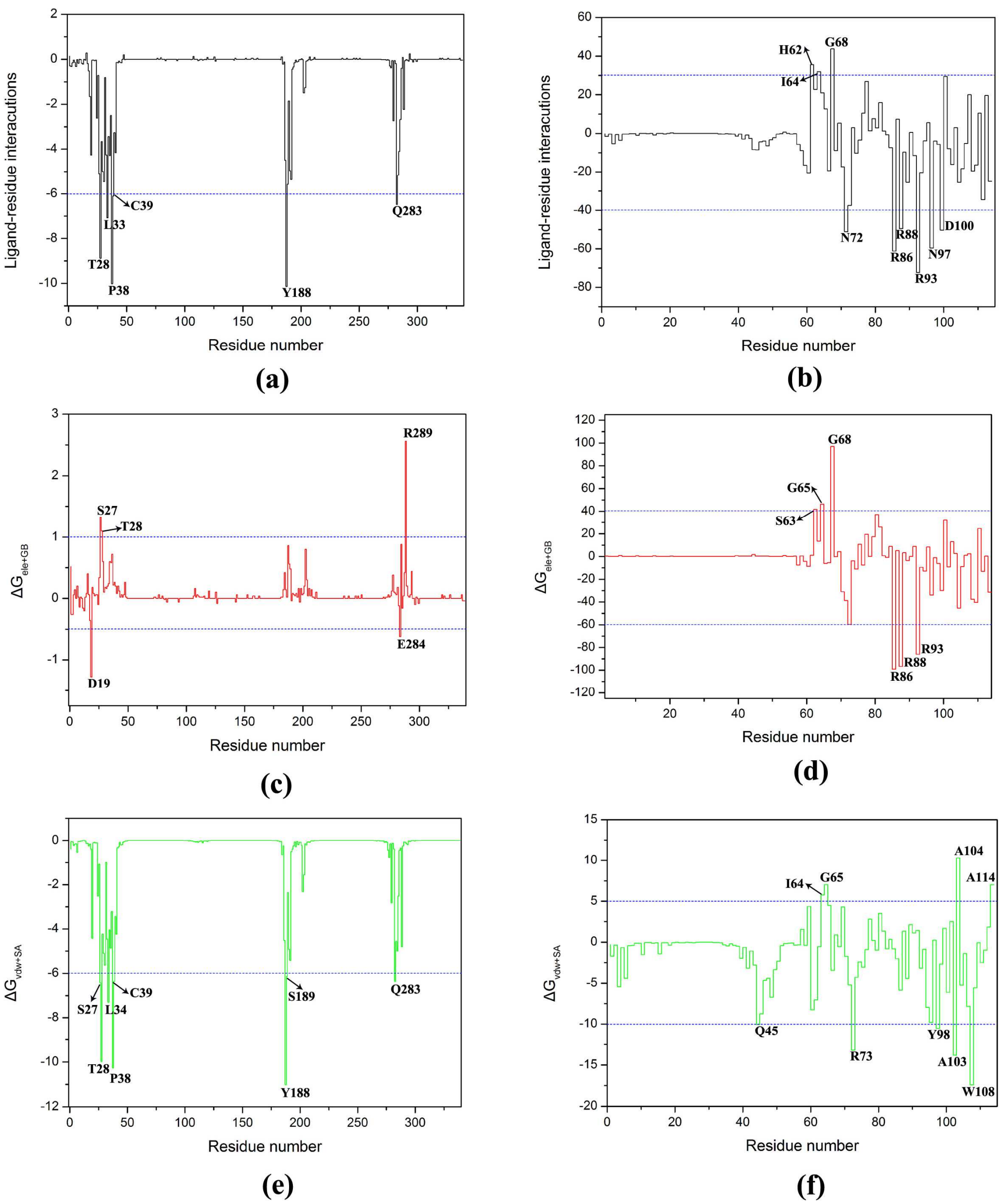

(a) (b)

(c) (d)

(e) (f)

Figure 8

Physical Chemistry Chemical Physics Accepted Manuscript

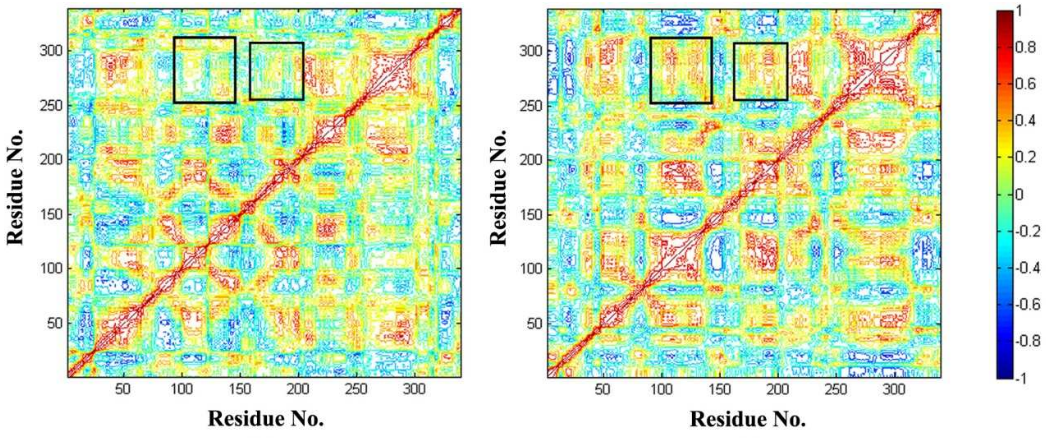

(a) **(b)**

Figure 9

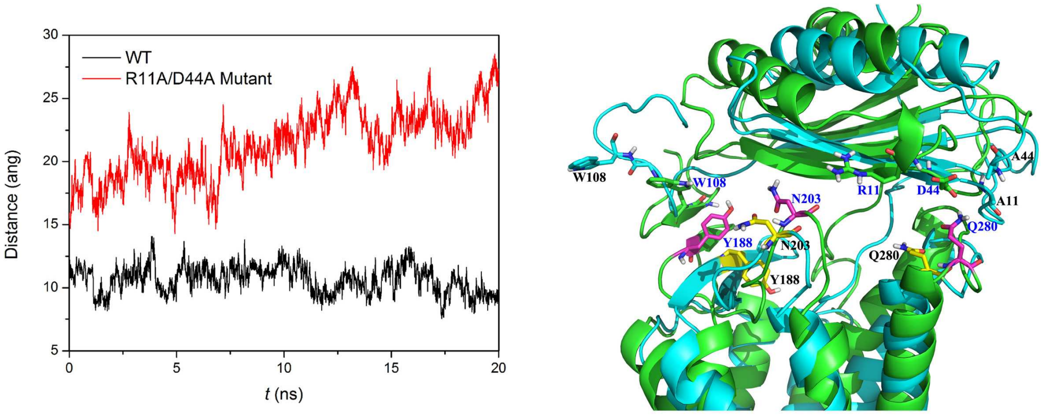

(a) **(b)**

Figure 10

Physical Chemistry Chemical Physics Accepted Manuscript

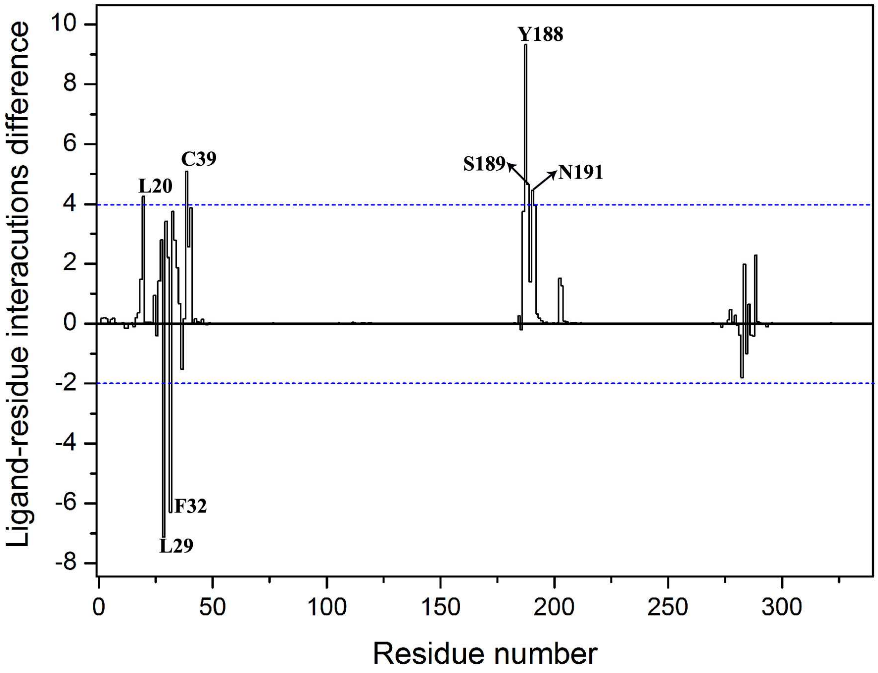

Figure 11

Physical Chemistry Chemical Physics Accepted Manuscript